Early-Age Stress and Pressure Developments in a Wellbore Cement Liner: Application to Eccentric Geometries

Thomas Petersen
Department of Civil and Environmental Engineering, Massachusetts Institute of Technology, Cambridge, MA 02139

Franz-Josef Ulm[1]
Department of Civil and Environmental Engineering, Massachusetts Institute of Technology, Cambridge, MA 02139

This paper introduces a predictive model for the stress and pressure evolutions in a wellbore cement liner at early ages. A pressure state equation is derived that observes the coupling of the elastic changes of the solid matrix, the eigenstress developments in the solid and porespaces, and the mass consumption of water in course of the reaction. Here, the transient constitution of the solid volume necessitates advancing the mechanical state of the poroelastic cement skeleton incrementally and at constant hydration degree. Next, analytic function theory is employed to assess the localization of stresses along the steel–cement (SC) and rock–cement (RC) interfaces by placing the casing eccentrically with respect to the wellbore hole. Though the energy release rate due to complete debonding of either interface is only marginally influenced by the eccentricity, the risk of evolving a microcrack along the thick portion of the sheath is substantially increased. Additionally, it is observed that the risk of microannulus formation is principally affected by the pressure rebound, which is engendered by the slowing reaction rate and amplified for rock boundaries with low permeability. [DOI: 10.1115/1.4034013]

1 Introduction

To maintain the benefits of natural gas as a safe transition energy source, drilling contractors must ensure that wells remain sealed during construction and operation. Accordingly, a cement barrier is placed into the annular region between the steel production casing and the wellbore hole. Nonetheless, Ingraffea et al. note that in Pennsylvania 6.2% (1.0%) of unconventional (conventional) wells drilled between 2000 and 2012 have compromised cement liners [1]. Moreover, it is known that early-age shrinkage phenomena and pore pressure developments are primary contributors to sheath failure: After placement, the curing cement undergoes pore pressure changes, chemical shrinkage phenomena, and eigenstress developments in the calcium–silicate–hydrate (CSH) gel—the binding phase of cement—that cause bulk volume changes [2,3]. Under restraint of the steel and rock boundaries, these volume changes can lead to stresses that impair the integrity of the sheath. A diagram of a typical wellbore system is presented in Fig. 1.

Current work at the molecular and mesoscales is revealing the fundamental driving forces of the cement volume changes and their relation to the CSH packing density [2]. Here, the construction of CSH gel as a system of colloidal particles has evinced net-attractive forces that follow the out-of-equilibrium dynamics of cement hydration. When left unconstrained, this eigenstress σ^*—a loading that produces no mechanical work—engenders a volume shrinkage of the gel. Additionally, the classification of confined water into free, constrained, and chemically bound water molecules [4] has elucidated the details of the H_2O kinetics during hydration and lends opportunity for improvements in modeling the hydrating cement phase morphology. Specifically, the hydration reaction produces a water sink in the paste that is driven by the stoichiometric demand of the cement chemical reaction and the adsorption of H_2O molecules onto the CSH gelpore surfaces [5]. This causes a drop in pore pressure Δp and, at the engineering scale, incites a fluid exchange between cement and rock formation.

An important design parameter, yet to be studied in connection with the early-age driving forces of cement volume change, is the eccentricity of the production casing with respect to the wellbore hole. In an experimental setup, Albawi investigated the fraction of interfacial debonding due to thermal cycling of specimens containing a centrically and an eccentrically located casing [4]. Using computer tomography, the eccentric casing (with a degree of eccentricity of $\mathcal{D}_e = 0.5$; at its thinnest portion, the sheath thickness is half the thickness of an equivalent concentric sheath) showed a greater fraction of debonding and subsequent creation of fluid channels. Related finite element simulations show that casing eccentricity can significantly enhance the risk of cement sheath failure [6], and it was noted that the added contribution of shear stress along the interfaces plays an acute role in crack initiation [7]. To the best of our knowledge, no analytic or semi-analytic

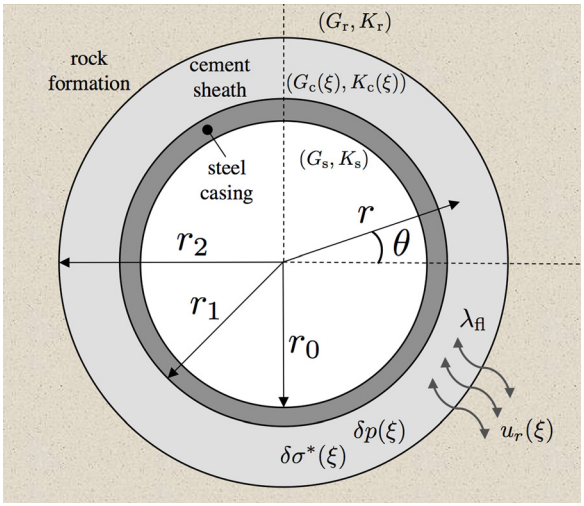

Fig. 1 Diagram of a wellbore cement liner

[1]Corresponding author.

Contributed by the Applied Mechanics Division of ASME for publication in the JOURNAL OF APPLIED MECHANICS. Manuscript received April 13, 2016; final manuscript received June 22, 2016; published online July 13, 2016. Editor: Yonggang Huang.

solution exists for the boundary value problem of a material domain confined by two eccentric, elastically deforming circular contours.

The present work offers sophistication in the design of wellbore cement liners: Section 2 develops a pressure state equation that balances the chemical and mechanical changes of the porosity with the external water supply from the adjacent rock formation. Section 3 is devoted to the derivation of an analytic solution of the stress state of the sheath, where the well-known complex variable method for plane elasticity is employed when the boundary contours are positioned eccentrically. The paper concludes in Sec. 4 by connecting the bulk stress calculations of the coupled chemoporomechanics model to the risk of fracture due to microannulus formation along the SC interface or the RC interface.

2 Incremental State Equations of Stress and Pressure in a Hydrating Cement Sheath

The incremental constitutive relations for the steel, cement paste, and rock are written, in order of appearance, as

$$\mathrm{d}\boldsymbol{\Sigma}(z) = \left(K_\mathrm{s} - \frac{2}{3}G_\mathrm{s}\right)\mathrm{tr}(\mathrm{d}\mathbf{E}(z)) + 2G_\mathrm{s}\,\mathrm{d}\mathbf{E}(z) \tag{1a}$$

$$\mathrm{d}\boldsymbol{\Sigma}(z) = \left(K_\mathrm{c} - \frac{2}{3}G_\mathrm{c}\right)\mathrm{tr}(\mathrm{d}\mathbf{E}(z)) + 2G_\mathrm{c}\,\mathrm{d}\mathbf{E}(z) + \mathrm{d}\Sigma^*(z)\mathbf{I} \tag{1b}$$

$$\mathrm{d}\boldsymbol{\Sigma}(z) = \left(K_\mathrm{r} - \frac{2}{3}G_\mathrm{r}\right)\mathrm{tr}(\mathrm{d}\mathbf{E}(z)) + 2G_\mathrm{r}\,\mathrm{d}\mathbf{E}(z) - b_\mathrm{r}\,\mathrm{d}p(z)\mathbf{I} \tag{1c}$$

where $z = x + iy = re^{i\theta}$ is the position vector in the complex plane, and K_d and G_d (where $d = \{\mathrm{s}, \mathrm{c}, \mathrm{r}\}$) denote the drained bulk and shear moduli, respectively. The concentric geometry is depicted in Fig. 1, where the material domains are rigidly connected along the interfaces $|z| = r_1$ and $|z| = r_2$. The internal loading of the cement paste drives the bulk stress development of the system, where $\mathrm{d}\Sigma^* = [(1-b)\mathrm{d}\sigma^* - b\,\mathrm{d}p]$ is the incremental change in the bulk eigenstress. Specifically, $\mathrm{d}\sigma^*$ accounts for the eigenstress in the solid phase and $\mathrm{d}p$ accounts for the pressure in the porespace, which are connected to the macroscale via the Biot coefficient, b [8]. It should further be noted that the growth of the solid volume during the cement hydration stiffens the material, such that K_c, G_c, and b are functions of the hydration degree ξ (see Fig. 2). As the pressure in the cement drops, the pressure in the rock in proximity to RC experiences a similar change. As a consequence, $\mathrm{d}p$ has been accounted for in Eq. (1c), where b_r is the Biot coefficient of the rock, herein assumed to be 1.

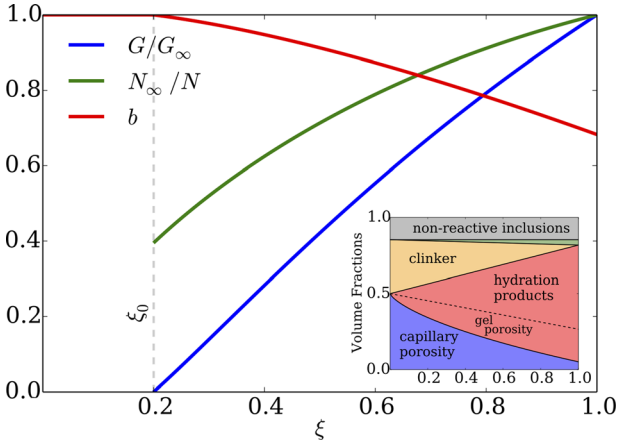

Fig. 2 The cement poroelastic constants in function of the hydration degree ($G_\infty = 11.1$ GPa and $N_\infty = 174.3$ GPa; see Table 2 in Appendix C for the calculation of the volume fractions and the upscaling of the poroelastic constants). The inset shows the evolution of the primary cement phases.

In the paragraphs to follow, we describe the origin of the pressure drop and connect it to the exchange of water with the rock formation.

2.1 Mass Balance of Water. The porespace of cement may broadly be categorized into macropores (capillary pores) and gelpores (formed in the CSH gel). Using the Lagrangian porosity ϕ, the total pore volume at a given hydration degree ξ and incremental loading $\mathrm{d}(p, \sigma^*, E_\mathrm{v})$ per unit initial reference volume, the fluid mass content is defined as $m = \rho_\mathrm{fl}\phi$, where ρ_fl denotes the fluid mass density [9]. Under drained and saturated conditions, the mass content of a representative elementary volume (REV) obeys

$$\frac{\mathrm{d}m}{\mathrm{d}t} = M_0 - \left(\delta m_\mathrm{hyd} + \delta m_\mathrm{surf}\right) \tag{2}$$

where the temporal change in fluid mass $\mathrm{d}m/\mathrm{d}t$ is driven by the difference in the external water supply, M_0, and the use of H_2O molecules in the creation of CSH ($\delta m_\mathrm{hyd} + \delta m_\mathrm{surf}$). To elaborate:

(i) The stoichiometric sink term δm_hyd, also termed water of constitution or structural water [10], refers to the observation that 1 g of cement requires between $\alpha_\mathrm{hyd} = 0.20$–$0.25$ g of water to produce CSH and calcium hydroxide products. Translated into volume fractions, this stoichiometric term thus reads

$$\frac{\delta m_\mathrm{hyd}}{\rho_\mathrm{fl}} = \alpha_\mathrm{hyd}\frac{\rho_\mathrm{c}}{\rho_\mathrm{fl}}f_\mathrm{c0}\frac{\mathrm{d}\xi}{\mathrm{d}t} = \beta_\mathrm{hyd}\frac{\mathrm{d}\xi}{\mathrm{d}t} \tag{3}$$

where $\rho_\mathrm{c}/\rho_\mathrm{fl} = 3.15$ is the cement-to-liquid mass density ratio, and f_c0 is the initial cement volume content. $\mathrm{d}\xi/\mathrm{d}t$ is the reaction rate, which is described by a hydration kinetics law (e.g., Ref. [11], see Appendix B). For $w/c = 0.45$, the stoichiometric sink term is on the order of $\beta_\mathrm{hyd} \approx 0.27$–$0.33$.

(ii) The adsorption sink term δm_surf was discovered by Powers [12] and has recently been quantified by reactive molecular simulations that traced the state of water in CSH [13]. The driving force of the adsorption sink term is the interaction potential, that is, the interparticle potential between the water adsorbed on the CSH gelpore surface and the bulk water in the gelpores, which in good approximation can be viewed as constant over the hydration process. Given the surface nature of the adsorption phenomena, the rate of water adsorption is scaled by the change of the surface area of the gel porosity, or more generally, by the specific surface area

$$\frac{\delta m_\mathrm{surf}}{\rho_\mathrm{fl}} = \alpha_\mathrm{C\text{–}w}n_{\mathrm{H_2O}}\frac{M_\mathrm{w}}{\rho_\mathrm{fl}}\frac{\mathrm{d}S_\mathrm{G}}{\mathrm{d}\xi}\frac{\mathrm{d}\xi}{\mathrm{d}t} = \beta_\mathrm{surf}\frac{\mathrm{d}\xi}{\mathrm{d}t} \tag{4}$$

where $\alpha_\mathrm{C\text{–}w}$ is the number of C–w bonds per surface, approximated at 2.4 bonds/nm^2; $n_{\mathrm{H_2O}}$ is the number of water molecules per bond ($\sim$10 $\mathrm{H_2O}$); $M_\mathrm{w} = 18$ g/mol is the molar mass of water; and S_G is the gelpore surface, which has been shown to increase almost linearly with the hydration degree [14,15]. A rough estimate of this term is provided by considering that the specific surface of cement paste $S_\mathrm{G}/\overline{\rho} \approx 168\,\mathrm{m}^2/\mathrm{g}$, as calculated from a colloidal mesoscale simulation for $w/c = 0.45$ paste [16], where $\overline{\rho} = 2\,\mathrm{g/cm}^3$ is the average paste density. Thus, $\beta_\mathrm{surf} \approx 0.12$–$0.43$, which means that the surface adsorption term is of the same order of magnitude as the stoichiometric sink term.

The change in the mass content accounted for in Eq. (2) is likewise obtained by considering the differential variation in the porosity and the fluid compressibility

Table 1 Model input parameters

Geometry (cm)			Elastic constants (GPa)				Newton coef. (s^{-1})	Eigenstress (MPa)	Eff. sink term	Ref. pressure (MPa)
r_0	r_1	r_2	G_s	K_s	G_r	K_r	λ_{fl}	$d\sigma^*/d\xi$	β_{eff}	p_0
10	11	16	78.7	144.9	15.4	33.3	$10(1) \times 10^{-6}$	147	0.1	40

$$\frac{dm}{\rho_{fl}} = d\phi|_{p,\sigma^*,E_v} + d\phi|_{\xi} + \frac{d\rho_{fl}}{\rho_{fl}}\phi \tag{5}$$

(i) The first term, $d\phi|_{p,\sigma^*,E_v}$, measures the change in the porosity due to the morphology of the REV phases—calculated at constant pressure p, eigenstress σ^*, and volumetric strain E_v. In poromechanics literature, this term is coined the chemical porosity [9,17]. Both the changes in the capillary and the gel porespaces contribute to this term, such that the evolution of $\phi|_{p,\sigma^*,E_v}$ in function of ξ is depicted by the dashed contour in the inset of Fig. 2.

(ii) The second term, $d\phi|_{\xi}$, measures, at constant hydration degree, the change in porosity due to the loading of the pore–solid system. More specifically, it measures the deformation of the solid skeleton due to an infinitesimal increment of volume strain, pressure, and eigenstress loading $d(E_v, p, \sigma^*)$ [9].

(iii) The final term $(d\rho_{fl}/\rho_{fl})\phi$ quantifies the mass change due to the compressibility of the fluid, where, under isothermal conditions, $d\rho_{fl}/\rho_{fl} = dp/k_{fl}$ with $1/k_{fl}$ being the fluid compressibility, i.e., the inverse of the fluid bulk modulus, k_{fl}.

Equating the mass balances described by Eqs. (2) and (5), one can write the state equation for the fluid mass content in cement paste under isothermal hydration as

$$b\frac{dE_v}{dt} + \frac{1}{N}\frac{d\sigma^*}{dt} + \frac{1}{M}\frac{dp}{dt} = k_c\frac{\rho_{fl}}{\eta_{fl}}\frac{\nabla^2 p}{M} - \frac{1}{\tau_{hyd}}\beta_{eff} \tag{6}$$

where ξ has passed the solid percolation threshold ξ_0, and $dp/dt = 0$ otherwise. The first term on the left-hand side (l.h.s.) of the equation quantifies the effect on the porespace due to an incremental bulk volume strain dE_v of the REV as per definition of the Biot coefficient $b(\xi)$. The second term on the l.h.s. models the effect of the eigenstress development in the CSH gel, where $N(\xi)$ is the corresponding Biot modulus of the solid matrix. The third term on the l.h.s. accounts for the change in pore pressure and its influence in compressing both the solid matrix and the fluid in the macro- and gelpores, $1/M(\xi) = 1/N + \phi/k_{fl}$. Finally, the terms on the right-hand side of the equation quantify, in order of appearance, the Laplacian (∇^2) of the pore pressure and the effective water sink. Here, k_c, ρ_{fl}, and η_{fl} are the cement permeability, fluid density, and fluid viscosity, respectively, while $\tau_{hyd} = (d\xi/dt)^{-1}$ is the characteristic time of cement hydration, dictating the rate of water consumption by the reaction. The effective sink term quantifies the combined effect of the physicochemical changes to the cement system: the stoichiometric water demand, the adsorption of water to the gelpore surfaces, and the growth of the solid skeleton: $\beta_{eff} = \beta_{hyd} + \beta_{surf} + d\phi|_{p,\sigma^*,E_v}/d\xi$.

2.2 Simplifying Assumption of Uniform Bulk Eigenstress Development. Once the pressure state equation (Eq. (6)) is applied to the boundary value problem of the cement sheath, the pore pressure varies according to the restraints and flux conditions of the steel and the rock interfaces. As the cement contracts or expands, the difference in the resistance of the steel and the rock produces gradients in strain. Nonetheless, a uniform loading of a concentric annular geometry results in a uniform volumetric strain across the cement domain. This is not the case for an eccentrically placed casing, where a gradient in E_v develops due to the nonuniform distribution of hydrating matter around the casing. Additionally, the no-flux boundary condition along the steel and permeable boundary of the soil causes fluid to travel into the cement sheath only along the outer interface upon water consumption by the reaction. Thus, a gradient in pressure is necessitated along RC.

Yet, the coupling of Eq. (6) to the macroscopic stress field is vastly simplified without loss of predictive power, if, in good approximation, the solid eigenstress and pressure developments can be assumed to develop uniformly. More precisely, we are enabled to apply the effective bulk eigenstress $d\Sigma^*(\xi) = (1-b)d\sigma^*(\xi) - b\,dp(\xi)$ directly along the boundary contours to calculate the equivalent stress field of the domain.

Small-to-moderate eccentricities of the casing maintain a mean stress field that is approximately uniform. By inspecting the stress state in the cement due to a uniform increment $d\Sigma^*$ and $\mathcal{D}_e = 0.8$, where the derivation of the stress state is presented in Sec. 3 and the input parameters are presented in Table 1, the radial and tangential stresses varied by ~25% of the applied load, while the mean stress varied by less than 2% over the cement body. Though the stiffness of the cement and rock may differ from the values chosen, model results by varying these parameters showed no appreciable growth in the mean stress gradient relative to the radial gradients of Σ_{rr} and $\Sigma_{\theta\theta}$. Consequently, E_v may reasonably be considered uniform without incurring error beyond the uncertainty posed by the model parameters.

Because the eigenstrain development of the CSH gel phase is an intrinsic property of the cement and the mix design is assumed homogeneous, it remains only to outline the conditions that render the spatial variations in the pressure negligible to ensure $d(\sigma^*, p, E_v)$ as approximately uniform.

2.2.1 Two Key Time Scales. Isolating the pressure components of Eq. (6) and nondimensionalizing, the normalized diffusion length of the pressure within the sheath is revealed as $\delta_p(\xi) = \sqrt{\lambda_c \tau_{hyd}}/(r_2 - r_1)$. Here, $\lambda_c(\xi) = k_c(\xi)\rho_{fl}/\eta_{fl}$ is the hydraulic conductivity of the cement, $\tau_{hyd}(\xi)$ is the characteristic time of hydration, and $\delta_p \geq 1$ allows the pressure to be modeled as uniform in good estimation. It must be remembered that the permeability of the sheath k_c changes with the microtexture of the cement and is directly related to the capillary porosity [18–20]. Thus, near the beginning of the hydration reaction λ_c is large, rapidly equilibrating the pressure in the sheath. At later stages of the reaction when λ_c decreases, the hydration kinetics slow (i.e., τ_{hyd} becomes large) to further minimize developments of the pressure variations.

Instead of resolving the pressure field explicitly, the dynamics are further investigated by discretizing Darcy's law to model the flow of water between the formation and the sheath

$$u_r^{fl} = \lambda_{fl}(p(r = r_2, t) - p_0) \tag{7}$$

where p_0 is the far-field formation pressure, and the above Newton coefficient depends on the flow characteristics of the cement and the rock via

$$\lambda_{fl} = \frac{\rho_{fl}}{\eta_{fl}}\left(\frac{l_c}{k_c} + \frac{l_r}{k_r}\right)^{-1} \tag{8}$$

where k_r is the permeability of the rock, and l_r (l_c) is the characteristic length scale of the radial pressure gradient in the rock

(cement). Moreover, the discretized expression for the fluid velocity allows us to relate the volume of the water consumed during the reaction $d\Omega_{sink}/dt \sim \pi(r_2^2 - r_1^2)/\tau_{hyd}$ and the volume of water entering along the RC boundary $d\Omega_{flux}/dt \sim \lambda_{fl} M r_2 2\pi/\rho_{fl}$. Comparison of these two quantities shows that the pressure dynamics depend on two characteristic time scales

$$\frac{d\Omega_{flux}}{d\Omega_{sink}} \sim \frac{2M\lambda_{fl}\tau_{hyd}}{\rho_{fl} r_2 \left(1 - r_1^2/r_2^2\right)} = \frac{\tau_{hyd}}{\tau_{fl}} \tag{9}$$

such that the characteristic time of hydration $\tau_{hyd} = dt/d\xi$ competes with the characteristic time of fluid influx $\tau_{fl} = \rho_{fl} r_2 (1 - r_1^2/r_2^2)/(2M\lambda_{fl})$ to change the pressure. Considering the parameters governing the fluid mobility in the cement and the formation and the hydration kinetics, several regimes of the pressure development emerge.

2.2.2 Sample Pressure Output of the Poromechanics Model. Table 1 and Fig. 2 provide the input parameters for the sample simulations presented in this paper; additional information on the calculation of the poroelastic constants is given in Appendix C. We chose to restrict ourselves to typical conditions encountered during primary cementing operations. In doing so, the parameters λ_{fl}, p_0, and ξ_0 were adjusted within the range of observable values to allow model resemblance with the pressure evolution of typical wellbore measurements. Figure 3 demonstrates the dependence of the pressure changes within the sheath on the ratio between the characteristic time of hydration and the characteristic time of mass exchange (τ_{hyd}/τ_{fl}):

(I) At early curing times, the rate of the hydration reaction is fast compared to the rate of recharge $\tau_{hyd}/\tau_{fl} \sim 10$–$100$, producing a rapid decrease in the cement pressure. Here, k_c is large and the water entering the cement sheath moves rapidly to equilibrate the pressure in the cement. It is thus the rock permeability that limits influx of water to the sheath, and the exchange coefficient in Eq. (8) tends toward $\lambda_{fl} \to (\rho_{fl}/\eta_{fl})(k_r/l_r)$. Because τ_{hyd} is small, the initial, rapid decrease in pressure is the dominant mechanism of the bulk eigenstress development. This is well exhibited by comparing the driving forces in Fig. 3(*a*) to the pressure changes in Fig. 3(*b*).

(II) At a degree of hydration of $\xi \approx 0.35$, the water demand of the reaction and the changes in the porespace are balanced by the Darcy flux into the annulus, such that a pressure minimum is realized. It is at this transition stage and during the early recovery of the pressure toward the equilibrium value of the far-field formation pressure that the uniformity of the pressure is most approximate. Nonetheless, the pressure has passed its minimum value, and hence, the local extremum in the loading conditions has expired. The percolation of a dense solid matrix decreases k_c, such that the pressure gradients are expected to evolve as a fringe along RC.

(III) For a more mature paste, the rate of the hydration reaction slows, and the pressure changes in the cement are principally affected by the influx of water, $\tau_{hyd}/\tau_{fl} \sim 10^3$–$10^6$. As a consequence, the decreased permeability of the cement drives variations in pressure. However, as the hydration reaction progresses, the incremental bulk eigenstress $d\Sigma^*$ is dominated by $d\sigma^*$ in the CSH gel phase. Again, we assume l_c to be small and limited by the dimension of the sheath and l_r to be large and controlled by the pressure drop in (I), such that the Newton coefficient is approximated as $\lambda_{fl} \to (\rho_{fl}/\eta_{fl})(k_r/l_r)$.

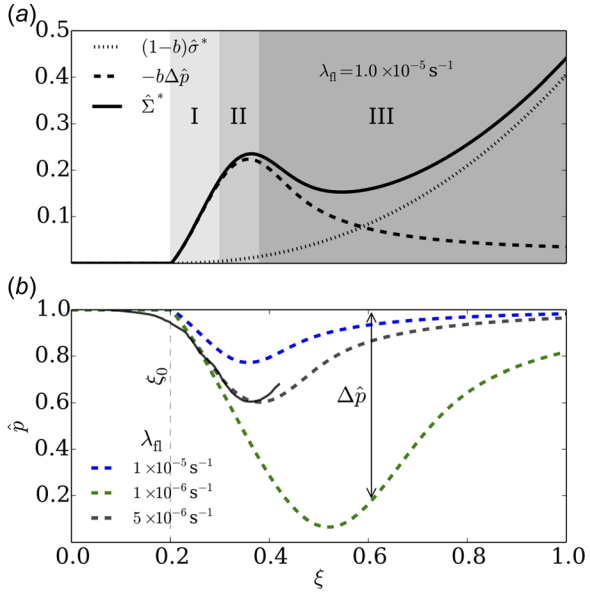

Fig. 3 Plots depicting the (*a*) driving forces of the bulk stress developments and (*b*) the pressure evolution $\hat{p} = p/p_0$ for low and high permeability formations. Herein, the solid eigenstress σ^* was assumed to evolve linearly with ξ. As a validation of concept, the black contours in (*b*) show smoothed, nondimensionalized pressure-log data for a well of undisclosed identity provided by Schlumberger (solid) and the pressure evolution simulated by our model (dashed) for a cement with *w/c* = 0.45.

For a low-to-moderately eccentric geometry, it is remarked that any pressure gradient in the radial direction far exceeds the gradient in the tangential direction: The distance over which the pressure varies is larger, $2\pi r_1 > r_2 - r_1$, and gradients develop principally due to the radial influx of water. As a consequence, an assumption of uniform radial pressure similarly implies tangential uniformity.

Accepting the conditions for the uniform treatment of the pressure and the CSH eigenstress development, the state equation in Eq. (6) can be simplified to the discrete form

$$Mb\frac{d\langle E_v\rangle}{d\xi} + \frac{M}{N}\frac{d\hat{\sigma}^*}{d\xi} + \frac{d\hat{p}}{d\xi} = \frac{\tau_{hyd}}{\tau_{fl}}(1 - \hat{p}) - \frac{M}{p_0}\beta_{eff} \tag{10}$$

where $\xi > \xi_0$ and $dp/d\xi = 0$ otherwise. The variables $\hat{p} = p/p_0$ and $\hat{\sigma}^* = \sigma^*/p_0$ are the normalized quantities of the pressure and solid eigenstress, and the brackets around E_v indicate its mean field value.

3 Stress and Pressure Evolutions

In the next segment of the paper, we couple the discrete version of pressure state equation (Eq. (10)) to the loading incurred by the boundary restraints. Though the solution assumes a linear elastic material behavior, nonlinearity arises due to the growth of the system volume, which is delineated by the boundary of the REV and the interface between solid and porespace. Hence, the out-of-equilibrium calculation of the mass growth is separated from the incremental loading of the solid (see Appendix of Ref. [5] for a more detailed thermodynamic reasoning).

3.1 The Case of a Concentrically Placed Casing. In a concentric geometry and for plane strain, the displacement solution, evaluated at a constant degree of hydration, is of the well-known form

$$d\mathbf{u}|_{\xi} = du_r \mathbf{e}_r = d\Sigma^*\left(C_1^* r + \frac{C_2^*}{r}\right) + dp\left(C_1^p r + \frac{C_2^p}{r}\right) \tag{11}$$

where $C_1^*(\xi)$, $C_2^*(\xi)$, $C_1^p(\xi)$, and $C_2^p(\xi)$ are constants determined by the boundary conditions and are given in Appendix A. Moreover, we have separated the mechanical response due to the

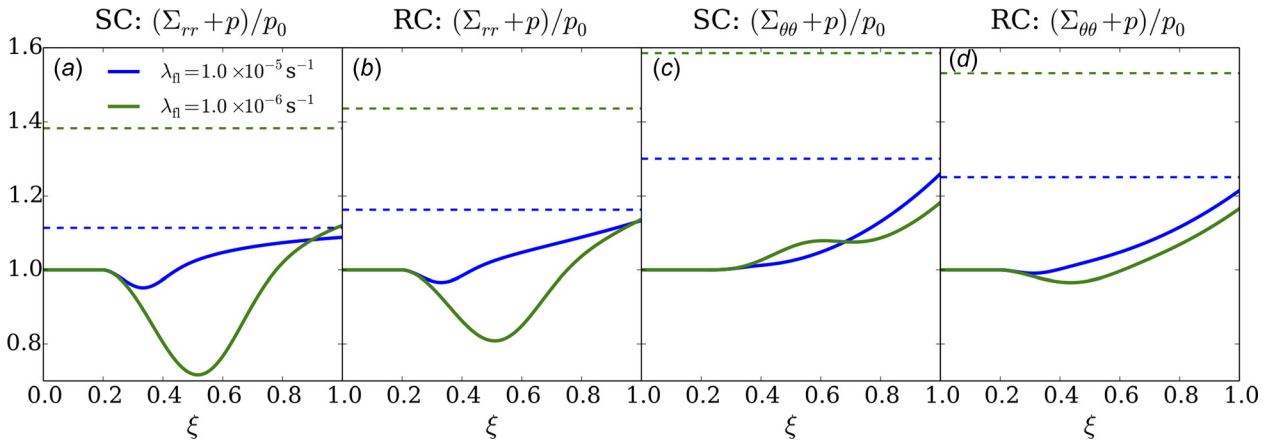

Fig. 4 Bulk effective radial ((*a*) and (*b*)) and tangential ((*c*) and (*d*)) stress development along the SC interface ((*a*) and (*c*)) and the RC interface ((*b*) and (*d*)). At complete hydration, a residual Δp remains in the system. Thus, the dashed contours show the asymptotic values of the effective stress, once the pressure has fully recovered to the reference value $p = p_0$.

loading increments of the bulk eigenstress and pressure, because the SC and RC interfaces differ in their drainage. Substituting the volumetric strain, $dE_v|_\xi = 6(d\Sigma^* C_1^* + dp\, C_1^p)$, into the pressure equation (Eq. (10)) allows the incremental change in pressure to be calculated as

$$d\hat{p}|_\xi = \frac{d\xi}{D^p+1}\left\{\frac{\tau_{hyd}}{\tau_{fl}}(1-\hat{p}) - \frac{M}{p_F}\beta_{eff} - \left(D^* + \frac{M}{N}\right)\frac{d\hat{\sigma}^*}{d\xi}\right\} \quad (12)$$

where $D^p = (C_1^p - 6b^2MC_1^*)$ and $D^* = (6b(1-b)MC_1^*)$. The results of iteratively updating first p and $\boldsymbol{\Sigma}$, and then the solid mass are displayed for the pressure in Fig. 3 and for the interfacial radial and tangential stresses in Fig. 4. The simulations were run for a more or less liberal exchange of water between rock and cement ($\lambda_{fl} = 1\times10^{-5}\,s^{-1}$ and $\lambda_{fl} = 1\times10^{-6}\,s^{-1}$).

The effective radial stress (Figs. 4(*a*) and 4(*b*)) in the sheath shows particular sensitivity to the dynamics of the pressure. Initially, during the period of accelerated hydration, a pressure drop is imposed on a relatively incompressible slurry; much of the system is still composed of a fluid mixture of water and clinker grains. As the matter hydrates, the growth of porous CSH gel increases the percolation and compressibility of the system. Finally, as the reaction rate slows and upon repressurization, the compressible cement matrix is placed into a state of residual tension. This phenomenon further increases the effective radial tensile stress beyond effects purely due to the eigenstress in the solid and porespace. In fact, if the system were to remain incompressible in course of the pressure evolution, no additional Cauchy stresses would be created. Instead, the hardening sheath is most vulnerable to microannulus formation—complete debonding of the interfaces—following the period of pressure recovery, after complete hydration. This is highlighted by the stress development in the less permeable system, where the extended regime of low pressure and delayed recovery heighten the final value of the residual tension.

The effective radial stress along SC and RC for $\xi = 1$ shows similar dependence on the rock permeability and stiffness parameters, respectively, displayed in Figs. 5(*a*) and 5(*b*). For a shrinking cement sheath, the adhesion to a stiff outer formation causes tensile stresses to develop along both interfaces. However, as is shown in Fig. 5(*a*) for large λ_{fl}, if G_r falls below the stiffness needed to resist the contraction of the sheath, the effective radial stress becomes compressive (i.e., $\Sigma_{rr} + p$ falls below the normalizing quantity p_0). Hence, under such conditions, a microannulus along RC prohibits debonding along SC. The contour plots generally show that stiff, impermeable rock boundaries place the cement sheath at greatest risk of failure. For highly nonconductive rock or when an external water supply is unavailable, the pore pressure remains below p_0 throughout hydration, helping balance the shrinkage of the solid skeleton due to σ^*. However, Figs. 5(*c*) and 5(*d*) show that the eventual recovery of the pressure leads to the most dangerous scenario, in which the radial tensile stresses increase by up to 60–70% of the reference pressure and effectively guarantee the failure of the liner.

As displayed in Figs. 4(*c*) and 4(*d*), the effective tangential stress $\Sigma_{\theta\theta} + p$ for $0 < \xi < 1$ is only marginally affected by the pressure drop as the steel and rock boundaries resist the constriction of the sheath around the casing. Contrary to Σ_{rr}, the increase in the macroscopic stress $\Sigma_{\theta\theta}$ is approximately balanced by the drop in pressure. Instead, the solid eigenstress is the primary agent causing the progressive increase in $\Sigma_{\theta\theta} + p$.

3.2 The Case of an Eccentrically Placed Casing. The boundary value problem of the cement sheath is complicated when casing eccentricity admits a loss of axisymmetry to the equilibrium equations. Jeffrey [21] is the first to have thoroughly treated the problem of a two-dimensional elastic solid bounded by eccentric circular contours, and his solution admits any prescriptions of traction along the boundaries so long as they are known and can be expressed as analytic functions of the polar argument. The difficulty in the elastic interface continuity conditions of the sheath is that they do not permit an a priori knowledge of the tractions. In the paragraphs to follow, we adopt the approach of seeking $\boldsymbol{\Sigma}$ and $\mathbf{u}$ as series representations, where added care is made to satisfy the elastic response of the bonded steel and rock.

3.2.1 Stress and Displacement Under Conformal Mapping. In our two-dimensional analysis of the sheath, we resort to the well-known Muskhelishvili representation of the incremental stress field [22]

$$d\boldsymbol{\Sigma}: \begin{cases} d\Sigma_{rr} - i d\Sigma_{r\theta} = \overline{\phi(z)} + \phi(z) - z\phi'(z) - \dfrac{z}{\bar{z}}\psi(z) \\ d\Sigma_{\theta\theta} + i d\Sigma_{r\theta} = \overline{\phi(z)} + \phi(z) + z\phi'(z) + \dfrac{z}{\bar{z}}\psi(z) \end{cases} \quad (13)$$

where $\kappa = 3 - 4\nu$ in plane strain, ϕ and ψ are complex potentials holomorphic in the domain of interest, and an overbar denotes complex conjugation. The change in displacement in Cartesian coordinates is given by

$$d\mathbf{u}: 2G(du_x + i du_y) = \kappa\Phi(z) - z\overline{\Phi'(z)} - \overline{\Psi(z)} \quad (14)$$

where $\phi(z) = \Phi'(z)$ and $\psi(z) = \Psi'(z)$, and it is often more convenient to work with the differentiated form

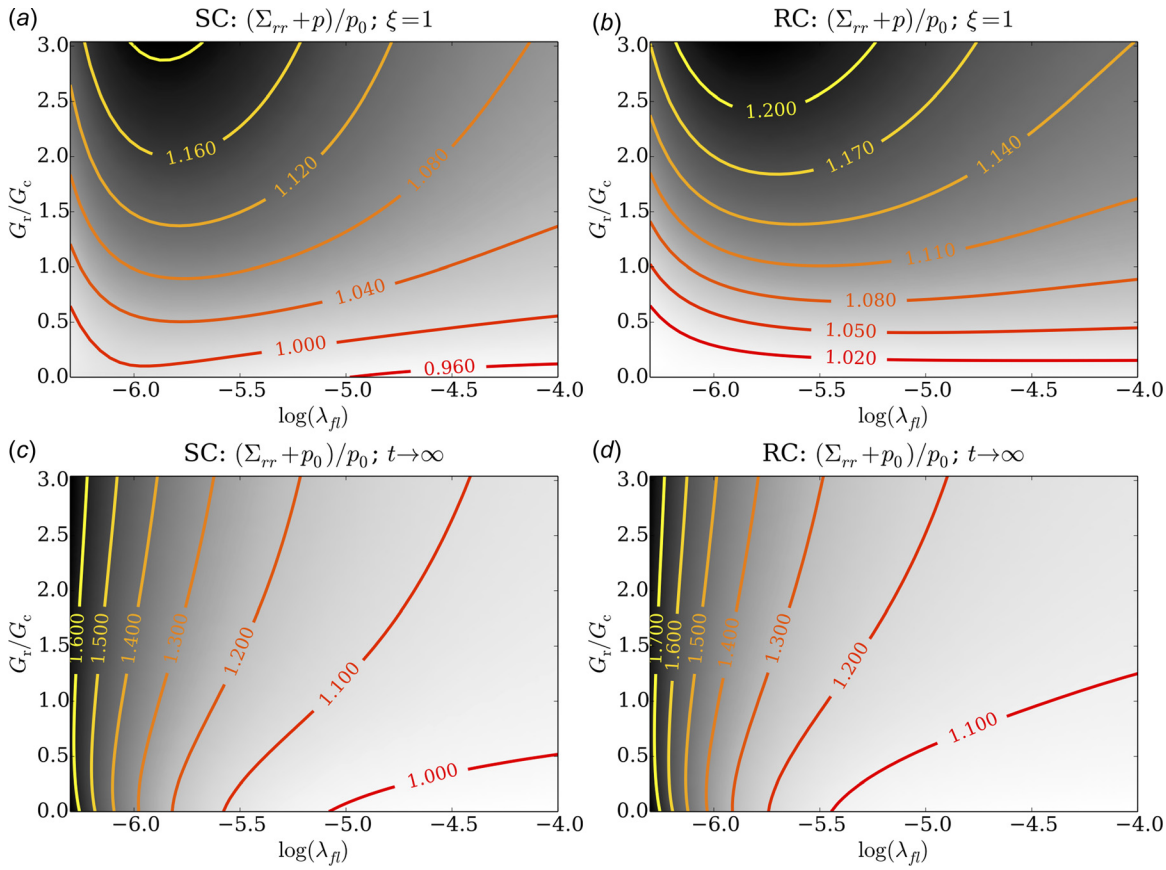

Fig. 5 Contour plots of the influence of the shear modulus ratio between rock and cement G_r/G_c and the Newton coefficient λ_{fl} on the effective radial stress along SC (left column of panel) and RC (right column) at complete hydration (top row) and once the pressure has completely recovered (bottom row). The casing placement is assumed concentric with the borehole.

$$\frac{2G}{-i\bar{z}}\frac{\partial}{\partial\theta}(du_x - idu_y) = \kappa\overline{\phi(z)} - \phi(z) + z\phi'(z) + \frac{z}{\bar{z}}\psi(z) \tag{15}$$

We map the cement interfaces onto circular contours centered at the origin. This allows for the complete description of the contours by their radial coordinate. In doing so, it is necessary to evaluate the stress and displacement of the steel, cement, and rock in separate coordinate systems, the z-, s-, and $\hat{z}$ - planes.

- The steel casing is placed at the center of the physical system in the z-plane. This defines the inner and outer surfaces of the casing by $|z| = r_0$ and $|z| = r_1$, respectively.
- The eccentric boundaries of the cement annulus are mapped onto concentric circles in the s-plane, defined by $|s| = \rho_1$ and $|s| = \rho_2$, where $s = \rho e^{i\vartheta}$.
- The wellbore hole is mapped to the $\hat{z}$-plane by translating the z-plane in the direction opposite the eccentricity, d, such that its surface is described by $|\hat{z}| = r_2$ and $\hat{z} = z - d = \hat{r}e^{i\hat{\theta}}$.

Movement between the reference and transformed domains of the cement is defined by

$$s = w(z) = \frac{\alpha + z}{\gamma + \beta z} \tag{16a}$$

$$z = \omega(s) = -\frac{\alpha - \gamma s}{1 - \beta s} \tag{16b}$$

and shown in Fig. 6. The radii of the transformed interfaces are calculated from the geometry of the physical system by

$$r_i \mapsto \rho_i = \frac{\sqrt{1 + (2\beta r_i)^2} - 1}{2\beta^2 r_i} \quad i = 1, 2 \tag{17}$$

where $\beta = d/\sqrt{(r_1^2 - r_2^2)^2 - 2d^2(r_1^2 + r_2^2) + d^2}$, $\alpha = \beta\rho_1^2/(1 - \beta^2\rho_1^2)$, $\gamma = (1 + \alpha\beta)$, and d is the eccentricity. Inserting the transformation into Eqs. (13) and (15) allows for the evaluation of stress and displacement in the s-plane

$$d\Sigma_{\rho\rho} + id\Sigma_{\rho\vartheta} = \overline{\varphi(s)} + \varphi(s) - \Gamma(s)\varphi'(s) - H(s)\chi(s) \tag{18a}$$

$$d\Sigma_{\vartheta\vartheta} + id\Sigma_{\rho\vartheta} = \overline{\varphi(s)} + \varphi(s) + \Gamma(s)\varphi'(s) + H(s)\chi(s) \tag{18b}$$

$$\frac{2G}{-i\overline{\omega(s)}}\frac{\partial}{\partial\theta}(du_x - idu_y) = \overline{\varphi(s)} + \varphi(s) - \Gamma(s)\varphi'(s) - H(s)\chi(s) \tag{18c}$$

where $\Gamma = s^2\overline{\omega}/\rho^2\overline{\omega'} = \gamma^2\rho^2/\alpha + (2\gamma - 1)e^{i\vartheta} - \alpha e^{i2\vartheta}$ and $H = s^2\omega'/\rho^2\overline{\omega'} = \sum_{n=0}^{\infty}\mathcal{H}_n e^{in\vartheta}$ and

$$\mathcal{H}_n = \begin{cases} \beta\rho^2 & \text{if } n = 0 \\ (-2n\beta^n + (n-1)\beta^{n-2}\rho^{-2} + (n+1)\beta^{n+2}\rho^2)\rho^n & \text{if } n > 0 \end{cases} \tag{19}$$

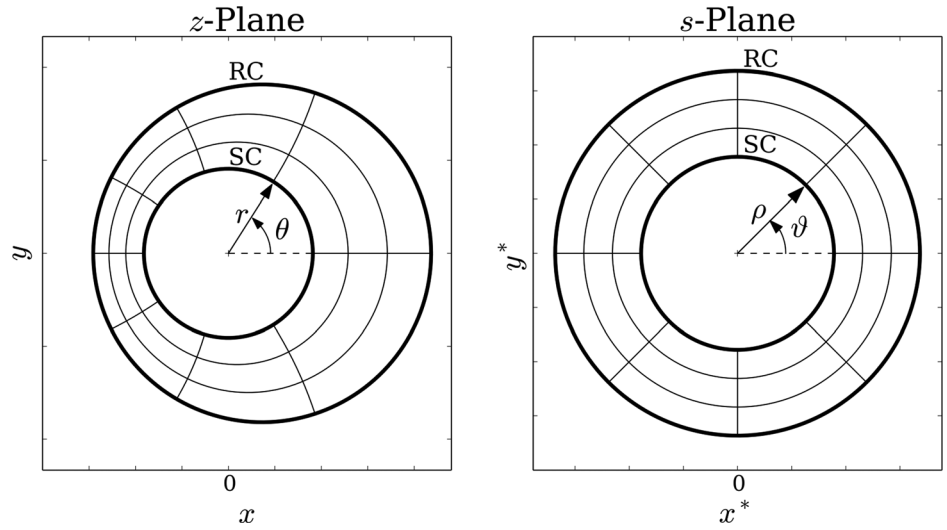

Fig. 6 Diagram of the bilinear transformation that maps the eccentric contours SC and RC in the *z*-plane to concentric contours in the *s*-plane

3.2.2 Boundary Conditions. The potentials of the Muskhelishvili formalism are sought as Laurent series

$$\phi_1(z) = \sum_{n=-\infty}^{\infty} A_n^{\mathrm{s}} z^n, \quad \psi_1(z) = \sum_{n=-\infty}^{\infty} B_n^{\mathrm{s}} z^n \quad \text{where } z \in S \tag{20a}$$

$$\varphi(s) = \sum_{n=-\infty}^{\infty} A_n^{\mathrm{c}} s^n, \quad \chi(s) = \sum_{n=-\infty}^{\infty} B_n^{\mathrm{c}} s^n \quad \text{where } \omega(s) = z \in C \tag{20b}$$

$$\phi_2(\hat{z}) = \sum_{n=-\infty}^{-1} A_n^{\mathrm{r}} \hat{z}^n, \quad \psi_2(\hat{z}) = \sum_{n=-\infty}^{-3} B_n^{\mathrm{r}} \hat{z}^n \quad \text{where } \hat{z} - d = z \in R \tag{20c}$$

where the positive powers of the potentials defining the rock stress have been truncated to keep the solution bounded as $z \to \infty$. We may further set $A_0^{\mathrm{r}} = 0$ and $B_{-2}^{\mathrm{r}} = 0$ on account that the far-field stress remains constant.

The total stress in the sheath is calculated by linearly superposing the real-valued stress Σ^* in $\rho_1 < |s| < \rho_2$ onto the boundary value problem. Complete continuity of traction and displacement ensures that both the normal and shear stresses generated by the shrinking cement specimen are transferred to the steel and rock. Solving for a divergence-free stress field, the boundary conditions are summarized as follows:

(1) The inner surface of the steel casing is assumed traction-free ($0 < \theta < 2\pi$)

$$\left.\overline{\phi_1} + \phi_1 - z\phi_1' - \frac{z}{\overline{z}}\psi_1 = 0\right\} \quad r = r_0 \tag{21}$$

(2) A rigid connection between steel and cement implies traction and displacement continuity along SC ($r = r_1$, $0 < \theta < 2\pi$ and $\rho = \rho_1$, $0 < \vartheta < 2\pi$)

$$\overline{\phi_1} + \phi_1 - z\phi_1' - \frac{z}{\overline{z}}\psi_1 = \overline{\varphi} + \varphi - \Gamma\varphi - H\chi + \mathrm{d}\Sigma^*|_\xi \tag{22a}$$

$$\overline{\phi_1} - \phi_1 - z\phi_1' - \frac{z}{\overline{z}}\psi_1 = G_{\mathrm{s}}/G_{\mathrm{c}}[\overline{\varphi} - \varphi - \Gamma\varphi - H\chi] \tag{22b}$$

(3) A rigid bond of the cement to the wellbore hole implies traction and displacement continuity along RC ($\hat{r} = \hat{r}_2$; $0 < \hat{\theta} < 2\pi$ and $\rho = \rho_2$, $0 < \vartheta < 2\pi$)

$$\overline{\phi_2} + \phi_2 - \left(\hat{z} + d\,e^{i2\hat{\theta}}\right)\phi_2' - \frac{\hat{z}}{\overline{\hat{z}}}\psi_2 - \mathrm{d}p = \overline{\varphi} + \varphi - \Gamma\varphi - H\chi + \mathrm{d}\Sigma^*|_\xi \tag{23a}$$

$$\overline{\phi_2} - \phi_2 - \left(\hat{z} + d\,e^{i2\hat{\theta}}\right)\phi_2' - \frac{\hat{z}}{\overline{\hat{z}}}\psi_2 = G_{\mathrm{r}}/G_{\mathrm{c}}[\overline{\varphi} - \varphi - \Gamma\varphi - H\chi] \tag{23b}$$

3.2.3 Matching the Boundary Arguments. It is readily noticed that the boundary conditions above are expressed as mutually non-orthogonal modes of $e^{ik\theta}$, $e^{ik\vartheta}$, and $e^{ik\hat{\vartheta}}$. With the help of Eq. (16*b*), the arguments along SC and RC are connected by

$$f(\vartheta) + if(\vartheta + \pi/2) = \begin{cases} e^{i\theta} = \omega(s = \rho_1 e^{i\vartheta})/r_1 & \text{if } r = r_1 \mapsto \rho = \rho_1 \\ e^{i\hat{\theta}} = (\omega(s = \rho_2 e^{i\vartheta}) - d)/r_2 & \text{if } \hat{r} = r_2 \mapsto \rho = \rho_2 \end{cases} \tag{24}$$

Furthermore, the analytic mapping of $s \mapsto z$ along $z \in$ SC allows the mode $e^{ik\vartheta}$ to be evaluated as a power series

$$e^{ik\vartheta} = \sum_{n=1}^{\infty} {}^{k}\eta_n e^{in\theta} \tag{25}$$

In evaluating the coefficients ${}^{k}\eta_n$, the Chebyshev polynomials of the first kind T_n allow higher modes $e^{in\theta}$ to be calculated from the relation in Eq. (24), such that the orthogonality condition of the polynomials gives

$$\begin{aligned} {}^{k}\eta_n &= -\frac{2}{\pi}\int_0^{\pi} \cos(k\vartheta) T_n\big(f(\vartheta)\big)\frac{\mathrm{d}\theta}{\mathrm{d}\vartheta}\mathrm{d}\vartheta \\ &\approx \frac{2}{N}\sum_{m=0}^{N} \cos(k\vartheta_m) T_n(f(\vartheta_m)) \end{aligned} \tag{26}$$

Here, the discrete approximation is evaluated at the abscissas $\vartheta_m = \pi(m - 1/2)/N$, and $k \ll N$ is required to achieve an accurate result. The same procedure is used to match modes of the $\hat{z}$ and s coordinate systems along RC (i.e., $e^{ik\vartheta} = \sum_{n=1}^{\infty} {}^{k}\hat{\eta}_n e^{in\hat{\theta}}$).

The remaining calculation of the stress state proceeds in the usual manner, where the series relations of the boundary conditions—now expressed solely using the modes $e^{in\vartheta}$ —are truncated upon convergence to produce a system of equations that determine the coefficients in Eqs. (20*a*)–(20*c*).

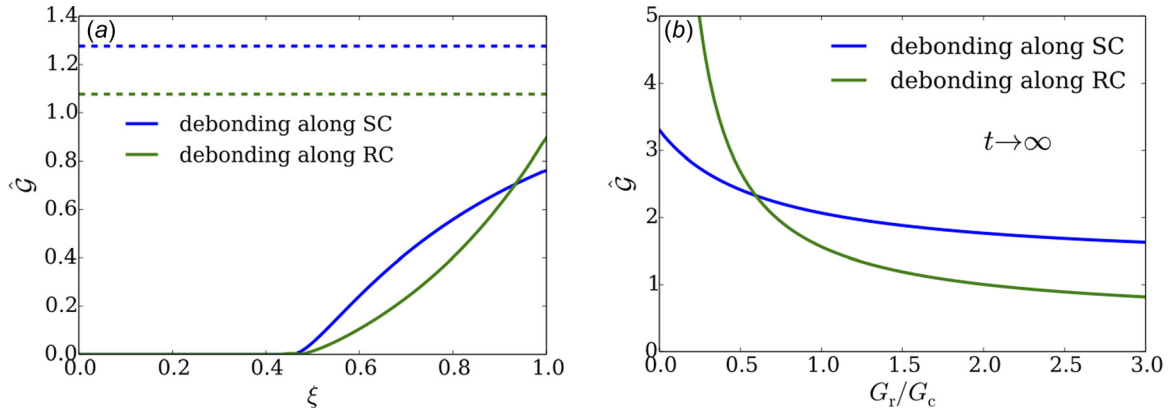

Fig. 7 (*a*) The evolution of the energy release rate for a vertically propagating microannulus in a concentric geometry for $\lambda_{fl} = 1 \times 10^{-5}$ s^{-1}; values normalized by $\hat{\mathcal{G}} = \mathcal{G}G_c^{\infty}/2\pi r_i \Sigma_{rr}^{\infty 2}$, where $i = 1$ along the SC and $i = 2$ along RC. The dashed contours show the energy release rate once the pressure has fully recovered. (*b*) The normalized energy release rate at $t \to \infty$ in function of the rock-to-cement shear modulus ratio.

4 Energy Release Rate Due to the Formation of a Microannulus

For common rock-to-cement stiffness ratios, the eccentricity of the boundaries will produce an increase (decrease) in the effective stress along the thick (thin) portion of the liner for an increment of loading. Here, the increase along the thick portion generally ranges between 10% and 20%, and is spread across a large fraction of the interface, whereas the drop in stress along the thin portion is more significant and spatially concentrated. Additionally, the loss of axisymmetry entails the creation of shear stresses $\Sigma_{r\theta}$ that concentrate near the rock boundary; the rigid body displacement of the steel casing with respect to the wellbore hole reduces $\Sigma_{r\theta}$ along SC.

The design of wellbore liners has traditionally been framed in the context of stress–strength-based failure criteria [6,23,24]. However, a recent spurt in research is shifting the design paradigm of liners toward predictive poromechanical fracture models [5,7,25,26]. Wang et al. [26], for instance, analyzed crack tunneling by loading the inner surface of the steel casing, and Petersen and Ulm [27] analyzed the early-age radial fracture in a cement sheath. A fracture design of setting cement requires the energy release rate $\mathcal{G}$ to be compared to the fracture energy $\mathcal{G}_{cr}$, for which the rate of evolution depends on the hydration degree as $d\mathcal{G}_{cr}/d\xi \sim 1/\xi$ [28] and we expect the interfacial fracture energy along SC and RC to show a similar trend.

Using Clapeyron's formula, the risk of failure of the liner due to microannulus formation is stated using the following fracture criterion:

$$\mathcal{G} = -\frac{\partial \mathcal{E}_{pot}}{\partial \Gamma} = \frac{\partial \mathcal{W}}{\partial \Gamma} = \int_{\partial\Omega} \frac{d\mathcal{G}}{ds}\, ds \leq \mathcal{G}_{cr} \tag{27}$$

In the above equation, the release of potential energy $\partial\mathcal{E}_{pot}$ in creating new crack surface area $\partial\Gamma$ may equivalently be regarded as the work done on the crack surfaces $\partial\mathcal{W}$ to reverse the infinitesimal fracture process. Hence, $d\mathcal{G}/ds$ is the distribution of work done along the boundary $\partial\Omega$ to bring the two fractured surfaces back together. Fracture is substantiated when $\mathcal{G}$ equals the interface toughness $\mathcal{G}_{cr}$. Therefore, with the requirement that the interfaces are in tension $(\Sigma(r_i) + \Delta p(r_i)) > 0$, we obtain for a drained fracture process

$$\mathcal{G} = \begin{cases} \dfrac{1}{2}\displaystyle\int_{\partial\Omega} [(\Sigma(r) + \Delta p \mathbf{I}) \cdot \mathbf{e}_r] \cdot \left| \mathbf{u}_0^s - \Delta p \frac{r_1}{\varkappa_s} \mathbf{e}_r \right| ds & \text{if } r = r_1 \\ \dfrac{1}{2}\displaystyle\int_{\partial\Omega} [(\Sigma(r) + \Delta p \mathbf{I}) \cdot \mathbf{e}_r] \cdot \left| \mathbf{u}_0^r - \Delta p \frac{r_2}{\varkappa_r} \mathbf{e}_r \right| ds & \text{if } \hat{r} = r_2 \end{cases} \tag{28}$$

where the term in the absolute value brackets measures the crack opening displacement. Hence, $\mathbf{u}_0^s$ ($\mathbf{u}_0^r$) is the displacement of the debonded inner (outer) sheath boundary with respect to the position before setting. The displacement must also account for the effects of a fluid pressure p acting on the newly created surfaces, such that the fractured steel (rock) interface displaces by $\Delta p\, r_1/\varkappa_s$ ($\Delta p\, r_2/\varkappa_r$).[1]

In Fig. 7(*a*), we display the progression of $\hat{\mathcal{G}}$ corresponding to the evolution of $\Sigma_{rr} + p$ in Fig. 4 for $\lambda_{fl} = 1 \times 10^{-5}$s^{-1} and we have adopted the normalization, $\hat{\mathcal{G}} = \mathcal{G}G_c^{\infty}/2\pi r_i \Sigma_{rr}^{\infty 2}$, where G_c^{∞} and Σ_{rr}^{∞} are the terminal values ($t \to \infty$; $\Delta p = 0$) of the cement shear modulus and the effective radial stress, respectively, and $2\pi r_i$ ($i = 1, 2$) is a measure of the crack length. In the plot, $\hat{\mathcal{G}}$ increases rapidly upon entering the tensile stress regime and achieves normalized values ~1.0–1.4 upon recovery to the formation pressure (indicated by the dashed lines). Here, it is remarked that the pressure recovery more drastically amplifies the energy release rate along SC. Next, Fig. 7(*b*) shows $\hat{\mathcal{G}}$ at $t \to \infty$ in function of G_r/G_c, where a low rock stiffness increases the system's compliance and, as a consequence, the normalized energy release rate. This must be contrasted with the reduced effective stresses entailed by the soft system (displayed in Fig. 5), such that the dimensional quantity $\mathcal{G}$ typically increases for larger G_r.

To quantify the increased risk posed by casing eccentricity, Fig. 8 shows the distribution of work done along SC and RC to reverse a microannulus, i.e., the integrands written in Eq. (28), which have been normalized with respect to the uniform distribution of the concentric geometry.[2] While the ~10% increase in work done along the thicker portion of the annulus along RC (Fig. 8(*b*)) coincides with the increase in the radial stress distribution, it is counterintuitive to observe a reduction of $d\mathcal{G}/d\theta$ along the entirety of SC for large eccentricities (Fig. 8(*a*)). In other words, casing eccentricity can reduce the risk of complete debonding along SC. Next, the increased risk of crack initiation is aptly quantified by considering the presence of a small flaw or microcrack along either interface, where the crack length is much smaller than the thicknesses of the casing and the sheath, $l \ll r_1 - r_0 < r_2 - r_1$. For such a crack, we can neglect the influence of the curvature of the boundaries, such that the condition of a crack between two semi-infinite material half-spaces can be assumed. The analytic behavior of such interface cracks is well

[1] $\varkappa_s$ and $\varkappa_r$ are the effective stiffnesses of the steel and rock, respectively (see Appendix A).

[2] It should be noted that the analytical calculation of the energy release rate for an in-plane crack that is only partially debonded is a complicated two-mode fracture process, and it is further unclear whether the crack will follow along the interface or kink out into the cement. Nonetheless, Lecampion et al. provide numerically tabulate results for cracks of partial azimuthal extent [29].

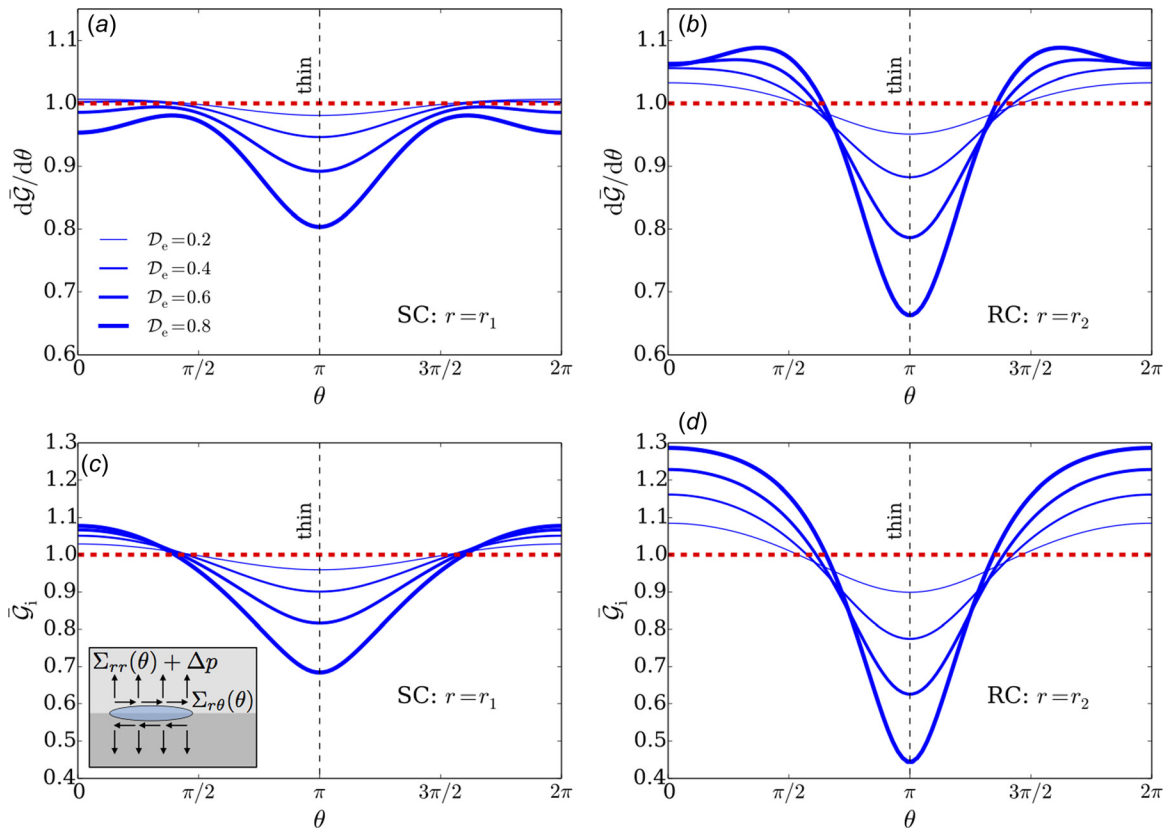

Fig. 8 The top panels show the distribution of work done along (*a*) SC and (*b*) RC to produce a microannulus along the respective interface for different degrees of casing eccentricity. The bottom panels display the energy release rate for a microcrack $\mathcal{G}_i$, i.e., the risk of crack initiation, along (*c*) SC and (*d*) RC. $d\bar{\mathcal{G}}/d\theta$ and $\bar{\mathcal{G}}_i$ have been normalized with respect to the uniform values in a concentric geometry.

understood [30], where the energy release rate for crack initiation scales as $\mathcal{G}_i \propto [(\Sigma_{rr}(\theta)+\Delta p)^2+\Sigma_{r\theta}(\theta)^2]$ and $\Sigma_{rr}+\Delta p>0$. The θ-dependence of crack initiation is plotted in Figs. 8(*c*) and 8(*d*) for SC and RC for the terminal stress states of our sample simulation. Normalized by the value of the concentric geometry, $\mathcal{G}_i$ increases for both SC and RC along the thick portion of the sheath, reaching maxima of ∼1.08 and ∼1.30, respectively. Hence, the introduction of casing eccentricity universally amplifies the prospect of crack formation.

To conclude, we display the relation between the maximum value of $\mathcal{G}_i$ along the interfaces and the rock-to-cement stiffness ratio in Fig. 9. The plot shows that an eccentrically placed casing increases the risk of crack initiation most drastically for soft formations, and it is noted that the normalized values for the low and high permeability scenarios differ due to the effects of their incremental loading histories. Interestingly, in decreasing the stiffness of the rock, the curve displaying $\mathcal{G}_i$ along SC for the highly permeable formation decreases to 1. This marks the ratio G_r/G_c at which the loading along SC transitions from tensile to compressive. Conversely, the increased repressurization at the end of hydration prevents a similar transition for $\lambda_{fl}=1.0\times10^{-6}\ s^{-1}$.

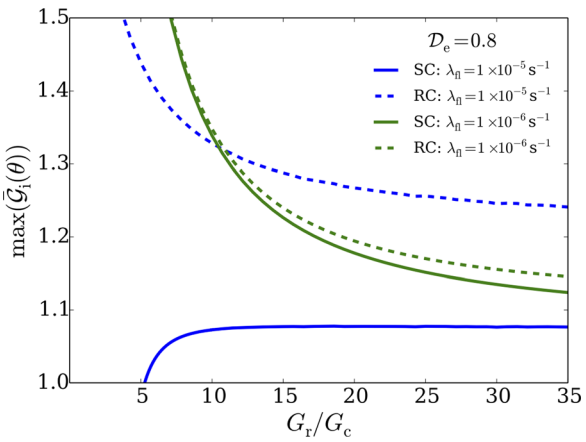

Fig. 9 The energy release rate for a microcrack along SC and RC $\bar{\mathcal{G}}_i(\theta)=\mathcal{G}_i^{ecc}(\theta)/\mathcal{G}_i^{cent}$ in function of different G_r/G_c

5 Conclusions

An analysis of the early-age pressure and stress evolution in a wellbore cement sheath has been conducted. We derived a pressure state equation by balancing the chemical and mechanical changes of the capillary porespace. Tracing the morphology of the phase volume fractions, and incorporating the loading due to eigenstress and pressure, we calculated the exchange of fluid with the adjacent rock formation. Though the model acts under the assumption of saturated, creep-free deformation, it nonetheless captures the underlying physics of the pressure and stress evolution. For a growing solid volume, the stress and pressure were advanced incrementally, which elucidated a critical phenomenon: the increase in cement compressibility in a lowered pressure environment poses a grave risk of microannulus formation upon repressurization. This highlights the system's permeability as the primary predictor of the final state of the radial effective stress.

Second, an analytic solution for the stress state of the sheath hydrating between two elastic eccentric boundaries was derived and used to infer the added risk of fracture. For a concentric geometry, it was found that high rock stiffness increases the effective radial stress along the boundaries, where $\mathcal{G}\propto(\Sigma_{rr}+\Delta p)^2$,

Table 2 Phase volume fractions and homogenized poroelastic constants for an REV at the characteristic length scales, levels I–III. The Biot coefficients and Biot moduli at the three scales are derived in Refs. [5] and [32].

	Level I (CSH solid + gelpores)	Level II (CSH gel + macropores)	Level III (hydrating matrix, CSH gel, macropores, and nonreactive inclusions)
Reference volume	$V_{\mathrm{I}} = V_{\mathrm{hp}}$	$V_{\mathrm{II}} = V_{\mathrm{hp}} + V_{\mathrm{w}}$	$V_{\mathrm{III}} = V_{\mathrm{II}} + V_{\mathrm{c}} + V_{\mathrm{nr}}$
Matrix fraction	$n_{\mathrm{I}} = \eta$	$n_{\mathrm{II}} = V_{\mathrm{hp}}/V_{\mathrm{II}}$	$n_{\mathrm{III}} = V_{\mathrm{II}}/V_{\mathrm{III}}$
Inclusion fraction	$\varphi = 1 - \eta$	$\phi_{\mathrm{M}}^{\mathrm{II}} = V_{\mathrm{w}}/V_{\mathrm{II}}$	$f_{\mathrm{inc}} = (V_{\mathrm{c}} + V_{\mathrm{nr}})/V_{\mathrm{III}}$
Total porosity	$\phi_0^{\mathrm{I}} = \varphi$	$\phi_0^{\mathrm{II}} = \phi_{\mathrm{M}}^{\mathrm{II}} + n_{\mathrm{II}}\varphi$	$\phi_0^{\mathrm{III}} = \phi_0^{\mathrm{II}}(1 - f_{\mathrm{inc}})$
Biot coefficient	$b_{\mathrm{I}} = 1 - K_{\mathrm{I}}/k_s$	$b_{\mathrm{II}} = 1 - K_{\mathrm{II}}/k_s$	$b_{\mathrm{III}} = b_{\mathrm{II}}$
Solid Biot modulus	$\frac{1}{N_{\mathrm{I}}} = \frac{b_{\mathrm{I}} - \phi_0^{\mathrm{I}}}{k_s}$	$\frac{1}{N_{\mathrm{II}}} = \frac{1}{k_s}\left[(1 - \phi_{\mathrm{M}}^{\mathrm{II}})(b_{\mathrm{I}} - \phi_0^{\mathrm{I}}) + (1 - b_{\mathrm{I}})\left(1 - \frac{K_{\mathrm{II}}}{K_{\mathrm{I}}} - \phi_{\mathrm{M}}^{\mathrm{II}}\right)\right]$	$\frac{1}{N_{\mathrm{III}}} = (1 - f_{\mathrm{inc}})\frac{1}{N_{\mathrm{II}}}$

though the simultaneous reduction in the system's compliance curbs the boundary displacement and consequently $\hat{\mathcal{G}}$ upon fracture. Next, the effect of casing eccentricity was inspected in the context of fracture. It was found that $\mathcal{G}$ for complete debonding of the interfaces is typically not substantially increased and in some cases even decreases along SC. Instead, there is a higher risk of crack initiation due to the localization of stresses and addition of the shear traction.

By shifting from stress–strength-based failure criteria toward fracture modeling and incorporating the chemoporous nature of the cement paste, the design of cement liners is progressed toward predictive, physics-based tools.

Acknowledgment

This work was financially supported by the National Science Foundation Graduate Research Fellowship Program and Schlumberger. Additionally, the authors would like to thank the researchers and engineers at the Schlumberger-Doll Research Center and the Schlumberger Riboud Product Center for their thoughts shared during weekly phone conferences.

Appendix A: Parameters Defining the Cement Stress Field in a Concentric Geometry

Defining the effective stiffnesses of the steel casing $\varkappa_{\mathrm{s}}$ and rock formation $\varkappa_{\mathrm{r}}$ as the uniform pressure acting along the outer and inner boundaries, respectively, to produce a unit of radial displacement, we write

$$\varkappa_{\mathrm{s}} = 2G_{\mathrm{s}}\frac{(G_{\mathrm{s}} + 3K_{\mathrm{s}})(\varpi_1^2 - 1)}{G_{\mathrm{s}}(3\varpi_1^2 + 1) + 3K_{\mathrm{s}}} \tag{A1a}$$

$$\varkappa_{\mathrm{r}} = 2G_{\mathrm{r}} \tag{A1b}$$

where $\varpi_1 = R_1/R_0$. Hence, the constants defining the stress state in the concentric geometric of the sheath are given as

$$C_1^* = -\frac{2G(1 - \varpi_2^2) + \varkappa_{\mathrm{S}} + \varpi_2^2\varkappa_{\mathrm{R}}}{\varkappa_{\mathrm{R}} + \varkappa_{\mathrm{S}}}C_2^* \tag{A2a}$$

$$C_2^* = \frac{3(\varkappa_{\mathrm{R}} + \varkappa_{\mathrm{S}})}{\Lambda} \tag{A2b}$$

$$C_1^p = -\frac{(\varkappa_{\mathrm{R}} + 2G)\varpi_2^2}{\varkappa_{\mathrm{R}} + \varkappa_{\mathrm{S}}}C_2^* \tag{A2c}$$

$$C_2^p = \frac{(2G + 6K + 3\varkappa_{\mathrm{R}})}{3(\varkappa_{\mathrm{R}} + \varkappa_{\mathrm{S}})}C_2^* \tag{A2d}$$

where $\varpi_2 = R_2/R_1$ and $\Lambda = 2(4G + 3K)(\varkappa_{\mathrm{R}} + \varkappa_{\mathrm{S}}) + (1 - \varpi_2^2)(3\varkappa_{\mathrm{R}}(\varkappa_{\mathrm{S}} - 2K) - 2G(3\varkappa_{\mathrm{S}} + \varkappa_{\mathrm{R}}) + 4G(3K + G))$.

Appendix B: Arrhenius Law

The hydration reaction is advanced using an Arrhenius type law of the form [31]

$$\frac{\mathrm{d}\xi}{\mathrm{d}t} = A(\xi)e^{-E_a/RT} = \tau_{\mathrm{hyd}}^{-1}(\xi, T); \quad A(\xi) = a\frac{1 - e^{-b\xi}}{1 + c\xi^d} \tag{B1}$$

where a, b, c, and d are parameters to be determined by fitting the above functional form to cement calorimetry data. The packing density—the volume ratio between hydrated cement and the hydration products—of the CSH gel is given by $\eta(\xi) = V_{\mathrm{hc}}/V_{\mathrm{hp}} \approx (\xi/\alpha)^{1/\beta}$, and $\beta = \ln(\xi_{\mathrm{lim}}/\xi_0)/\ln(\eta_{\mathrm{lim}}/\eta_0)$; $\alpha = \xi_0/\eta_0^{\beta} = 1/\eta_{\mathrm{lim}}^{\beta}$, where η_{lim} and η_0 are the limit packing density and the packing density at percolation, respectively. We assumed $\eta_{\mathrm{lim}} = 0.72$ and $\eta_0 = 0.50$ in our simulations. For the calculation of the evolution of the volume fractions, refer to Ref. [32].

Appendix C: Upscaling Procedure of a Three-Level Cement System

The elastic constants of the CSH gel, a granular, colloidal composite, are upscaled via a self-consistent scheme [33], where $K_{\mathrm{I}}/k_s = (4\eta G/g_s)(4G/g_s + 3(1 - \eta)r_s)$

$$\frac{G_{\mathrm{I}}}{g_s} = \frac{1}{2} - \frac{5}{4}(1 - \eta) - \frac{3}{16}r_s(2 + \eta) + \frac{1}{16} \times\sqrt{144(1 - r_s) - 480\eta + 400\eta^2 + 408r_s\eta - 120r_s\eta^2 + 9r_s^2(2 + \eta)^2}$$

and $r_s = k_s/g_s = 2(1 + \nu_s)/3(1 - 2\nu_s) > 0$. Next, the Mori–Tanaka scheme homogenizes the constants for a CSH gel matrix with capillary porosity using $K_{\mathrm{II}}/K_{\mathrm{I}} = (4(1 - \phi_M^{\mathrm{II}}))/(4 + 3\phi_M^{\mathrm{II}}r_{\mathrm{I}})$ and $G_{\mathrm{II}}/G_{\mathrm{I}} = [(8 + 9r_{\mathrm{I}})(1 - \phi_M^{\mathrm{II}})]/[8 + 9r_{\mathrm{I}} + 6\phi_M^{\mathrm{II}}(2 + r_{\mathrm{I}})]$, where $r_{\mathrm{I}} = K_{\mathrm{I}}/G_{\mathrm{I}}$ and $\phi_M^{\mathrm{II}} = (V_{\mathrm{g}} + V_{\mathrm{w}})/(V_{\mathrm{II}})$ [17]. Finally, we access the macroscale by incorporating rigid, slippery inclusions (representative of, e.g., silica flour), and the unhydrated clinker grains in a self-consistent scheme: The bulk and shear moduli are calculated as $K_{\mathrm{III}}/K_{\mathrm{II}} = [3r_{\mathrm{II}} + 4(G_{\mathrm{III}}/G_{\mathrm{II}})n_{\mathrm{III}}]/[3(1 - n_{\mathrm{III}})r_{\mathrm{II}}]$, and

$$\frac{G_{\mathrm{III}}}{G_{\mathrm{II}}} = \frac{1}{24}\frac{1}{(2 - 3n_{\mathrm{III}})}\left[8(3 - 2n_{\mathrm{III}}) - (15 - 24n_{\mathrm{III}})r_{\mathrm{II}} + \sqrt{9(8n_{\mathrm{III}} - 5)^2r_{\mathrm{II}}^2 + 48(11n_{\mathrm{III}}^2 - 29n_{\mathrm{III}} + 15)r_{\mathrm{II}} + 64(3 - 2n_{\mathrm{III}})^2}\right]$$

where $r_{\mathrm{II}} = K_{\mathrm{II}}/G_{\mathrm{II}}$ [34]. Herein, the bulk properties of the CSH solid were assumed $k_s = 49$ GPa and $g_s = 23.5$ GPa [35]. The

remaining relations are found in Table 2, where w = water, c = cement clinker, hp = hydration products, and nr = nonreactive inclusions.

References

[1] Ingraffea, A. R., Wells, M. T., Santoro, R. L., and Shonkoff, S. B. C., 2014, "Assessment and Risk Analysis of Casing and Cement Impairment in Oil and Gas Wells in Pennsylvania, 2000–2012," Proc. Natl. Acad. Sci., **111**(30), pp. 10955–10960.

[2] Masoero, E., Del Gado, E., Pellenq, R. J.-M., Yip, S., and Ulm, F.-J., 2014, "Nano-Scale Mechanics of Colloidal C–S–H Gels," Soft Matter, **10**(3), pp. 491–499.

[3] Bonett, A., and Pafitis, D., 1996, "Getting to the Root of Gas Migration," Oilfield Rev., **8**(1), pp. 36–49.

[4] Albawi, A., 2013, "Influence of Thermal Cycling on Cement Sheath, Integrity," Master's thesis, Faculty of Engineering Science and Technology, Department of Petroleum Engineering and Applied Geophysics, Norwegian University of Science and Technology, Trondheim, Norway.

[5] Ulm, F.-J., Abuhaikal, M., Petersen, T. A., and Pellenq, R. J.-M., 2014, "Poro-Chemo-Fracture-Mechanics…Bottom-Up: Application to Risk of Fracture Design of Oil and Gas Cement Sheath at Early Ages," *Computational Modelling of Concrete Structures*, CRC Press, Boca Raton, FL, p. 61.

[6] Nabipour, A., Joodi, B., and Sarmadivaleh, M., 2010, "Finite Element Simulation of Downhole Stresses in Deep Gas Wells Cements," SPE Deep Gas Conference and Exhibition, Society of Petroleum Engineers, Manama, Bahrain, Jan. 24–26, Paper No. SPE-132156-MS.

[7] Wang, W., and Taleghani, A. D., 2014, "Three-Dimensional Analysis of Cement Sheath Integrity Around Wellbores," J. Pet. Sci. Eng., **121**, pp. 38–51.

[8] Nur, A., and Byerlee, J. D., 1971, "An Exact Effective Stress Law for Elastic Deformation of Rock With Fluids," J. Geophys. Res., **76**(26), pp. 6414–6419.

[9] Coussy, O., 2004, *Poromechanics*, Wiley, Chichester, UK.

[10] Powers, T. C., and Brownyard, T. L., 1946, "Studies of the Physical Properties of Hardened Portland Cement Paste," Proc.-Am. Concr. Inst., **43**(9), pp. 249–336.

[11] Ulm, F.-J., and Coussy, O., 2001, "What Is a 'Massive' Concrete Structure at Early Ages? Some Dimensional Arguments," J. Eng. Mech., **5**(512), pp. 512–522.

[12] Powers, T. C., 1935, "Absorption of Water by Portland Cement Paste During the Hardening Process," Ind. Eng. Chem., **27**(7), pp. 790–794.

[13] Abdolhosseini Qomi, M. J., Krakowiak, K. J., Bauchy, M., Stewart, K. L., Shahsavari, R., Jagannathan, D., Brommer, D. B., Baronnet, A., Buehler, M. J., Yip, S., Ulm, F.-J., Van Vliet, K. J., and Pellenq, R. J.-M., 2014, "Combinatorial Molecular Optimization of Cement Hydrates," Nat. Commun., **5**, p. 4960.

[14] Thomas, J. J., Jennings, H. M., and Allen, A. J., 1998, "The Surface Area of Cement Paste as Measured by Neutron Scattering: Evidence for Two CSH Morphologies," Cem. Concr. Res., **28**(6), pp. 897–905.

[15] Barberon, F., Korb, J.-P., Petit, D., Morin, V., and Bermejo, E., 2003, "Probing the Surface Area of a Cement-Based Material by Nuclear Magnetic Relaxation Dispersion," Phys. Rev. Lett., **90**(11), p. 116103.

[16] Ioannidou, K., Krakowiak, K. J., Bauchy, M., Hoover, C. G., Masoero, E., Yip, S., Ulm, F.-J., Levitz, P., Pellenq, R. J.-M., and Del Gado, E., 2016, "Mesoscale Texture of Cement Hydrates," Proc. Natl. Acad. Sci., **113**(8), pp. 2029–2034.

[17] Dormieux, L., Kondo, D., and Ulm, F.-J., 2006, *Microporomechanics*, Wiley, Chichester, UK.

[18] Verbeck, G. J., and Helmuth, R. H., 1968, "Structures and Physical Properties of Cement Paste," 5th International Symposium on the Chemistry of Cement, Tokyo, Japan, Oct. 7–11, pp. 1–32.

[19] Taylor, H. F. W., 1997, *Cement Chemistry*, Thomas Telford, London.

[20] Powers, T. C., 1958, "Structure and Physical Properties of Hardened Portland Cement Paste," J. Am. Ceram. Soc., **41**(1), pp. 1–6.

[21] Jeffery, G. B., 1921, "Plane Stress and Plane Strain in Bipolar Co-Ordinates," Philos. Trans. R. Soc., A, **221**(582–593), pp. 265–293.

[22] Muskhelishvili, N. I., 1953, *Some Basic Problems of the Mathematical Theory of Elasticity: Fundamental Equations, Plane Theory of Elasticity, Torsion, and Bending*, J. R. M. Radok, trans., Noordhoff International Publishing, Groningen, The Netherlands.

[23] Thiercelin, M. J., Dargaud, B., Baret, J. F., and Rodriquez, W. J., 1998, "Cement Design Based on Cement Mechanical Response," SPE Drill. Completion, **13**(4), pp. 266–273.

[24] DeBruijn, G. G., Garnier, A., Brignoli, R., Bexte, D. C., and Reinheimer, D., 2009, "Flexible Cement Improves Wellbore Integrity in SAGD Wells," SPE/IADC Drilling Conference and Exhibition, Society of Petroleum Engineers, Amsterdam, The Netherlands, Mar. 17–19, Paper No. SPE-119960-MS.

[25] Ardakani, S. M., and Ulm, F.-J., 2013, "Chemoelastic Fracture Mechanics Model for Cement Sheath Integrity," J. Eng. Mech., **140**(4), p. 04013009.

[26] Wang, Z., Lou, Y., and Suo, Z., 2016, "Crack Tunneling in Cement Sheath of Hydrocarbon Well," ASME J. Appl. Mech., **83**(1), p. 011002.

[27] Petersen, T. A., and Ulm, F.-J., 2016, "Radial Fracture in a Three-Phase Composite: Application to Wellbore Cement Liners at Early Ages," Eng. Fract. Mech., **154**, pp. 272–287.

[28] Hoover, C. G., and Ulm, F.-J., 2015, "Experimental Chemo-Mechanics of Early-Age Fracture Properties of Cement Paste," Cem. Concr. Res., **75**, pp. 42–52.

[29] Lecampion, B., Bunger, A., Kear, J., and Quesada, D., 2013, "Interface Debonding Driven by Fluid Injection in a Cased and Cemented Wellbore: Modeling and Experiments," Int. J. Greenhouse Gas Control, **18**, pp. 208–223.

[30] Rice, J., 1988, "Elastic Fracture Mechanics Concepts for Interfacial Cracks," ASME J. Appl. Mech., **55**(1), pp. 98–103.

[31] Hellmich, C., Ulm, F.-J., and Mang, H. A., 1999, "Consistent Linearization in Finite Element Analysis of Coupled Chemo-Thermal Problems With Exo- or Endothermal Reactions," Comput. Mech., **24**(4), pp. 238–244.

[32] Petersen, T. A., 2015, "Chemo-Poro-Elastic Fracture Mechanics of Wellbore Cement Liners: The Role of Eigenstress and Pore Pressure on the Risk of Fracture," Master's thesis, Massachusetts Institute of Technology, Cambridge, MA.

[33] Constantinides, G., and Ulm, F.-J., 2007, "The Nanogranular Nature of C–S–H," J. Mech. Phys. Solids, **55**(1), pp. 64–90.

[34] Ortega, J. A., Gathier, B., and Ulm, F.-J., 2011, "Homogenization of Cohesive-Frictional Strength Properties of Porous Composites: Linear Comparison Composite Approach," J. Nanomech. Micromech., **1**(1), pp. 11–23.

[35] Qomi, M. J. A., Bauchy, M., Ulm, F.-J., and Pellenq, R., 2015, "Polymorphism and Its Implications on Structure-Property Correlation in Calcium-Silicate-Hydrates," *Nanotechnology in Construction*, K. Sobolev and S. P. Shah, eds., Springer, Cham, Switzerland, pp. 99–108.